




Effect of Ca²⁺ doping on the electronic charge density and magnetic properties of ZnFe₂O₄ spinel ferrites

M. Thavarani¹, M. Charles Robert^{2,*} , N. Pavithra¹, R. Saravanan³, Y. B. Kannan⁴, and S. Balaji Prasath²

¹Department of Physics, Sri Adi Chunchanagiri Women's College, Cumbum, Tamil Nadu, India

²Research Centre and PG Department of Physics, Hajee Karutha Rowther Howdia College, Uthamapalayam, Tamil Nadu, India

³Research Centre and PG Department of Physics, Madura College, Madurai, Tamil Nadu, India

⁴Department of Physics, Arumugam Pillai Seethai Ammal College, Tiruppattur, Tamil Nadu, India

Received: 30 September 2021

Accepted: 13 December 2021

© The Author(s), under exclusive licence to Springer Science+Business Media, LLC, part of Springer Nature 2021

ABSTRACT

The phase pure Ca²⁺-doped ZnFe₂O₄ spinel ferrite, synthesized by solvothermal method were analyzed using X-ray diffraction data. The structure factor corresponding to miller lattice planes and parameters like cell constants, anion positional parameter (O²⁻), etc., are calculated using Rietveld refinement strategy, considering cubic spinel structure. The cation distribution study reveals mixed spinel structure with both Ca²⁺ and Fe³⁺ ions occupying both tetrahedral A site and octahedral B site and Zn²⁺ occupying only at tetrahedral A site. The quantitative and visual electron bonding study reveals covalent bonding between A site ions and O²⁻ ions and ionic bonding between B site ions and O²⁻ ions for all the compositions and both are dominating for the composition Ca_{0.2}Zn_{0.8}Fe₂O₄. Also, the maximum entropy method-based electron density studies reveals that A–B interaction is maximum compared to A–A and B–B interactions and A–A interaction is the weakest one. The surface morphology using SEM shows spherical particle nature and energy dispersive X-ray analysis shows its stoichiometric compositions without any impurity elements. The magnetic properties are analyzed using vibrating sample magnetometer, which reveals the prepared sample with composition Ca_{0.2}Zn_{0.8}Fe₂O₄ show good ferromagnetic properties at room temperature. The observed saturation magnetization, remanent magnetization, coercivity and squareness ratio (M_r/M_s) for the composition Ca_{0.2}Zn_{0.8}Fe₂O₄ are 32.588 emu/g, 9.4265 emu/g, 407.98 gauss, and 28.95%, respectively. The present work reveals that Ca_{0.2}Zn_{0.8}Fe₂O₄ may be one of the best alternative low-cost and environment friendly semi-hard ferrite, useful in high-frequency device applications.

Address correspondence to E-mail: jothycharles@gmail.com

<https://doi.org/10.1007/s10854-021-07605-8>

Published online: 23 January 2022

1 Introduction

ferrites are ceramic-like ferromagnetic materials normally containing magnetic ions Fe^{3+} , which are classified by the formula MeFe_2O_4 with Me, a divalent and Fe, a trivalent cation [1]. Based on the magnetic properties, it can be classified as soft and hard ferrites. Though the saturation magnetization of ferrites is lesser than ferromagnetic alloys, both soft and hard ferrites have their industrial applications in large scale (both high and low frequency), because of its low price, high heat resistance and greater corrosion resistance [2]. Mn–Zn ferrites and Ni–Zn ferrites are examples of soft ferrites useful in high-frequency device applications above 1 MHz [3]. Cobalt ferrite is semi-hard ferrite mainly used for magnetostriction applications such as sensors and actuators [4, 5]. Strontium ferrites and Barium ferrites are hard ferrite type with high coercivity and remanence, useful for magnetic recording device applications as well as bio-diagnostics, bio-sensors, and bio-markers [6].

The spinel ferrites can be properly doped to get a particular magnetic property by the nature of the dopants and its concentration, cation distribution in both tetrahedral A site and octahedral B site and particle size reduction from micrometer to nanometer scale. The ionic radii of cations, chemical composition and mode of preparation of the sample mainly defines the cation distribution [7]. The electron density distribution analysis and the interaction between tetrahedral A site and octahedral B site is better explained based on the MEM electron density studies of some of the ferrites [8, 9]. Zinc ferrite is reported as normal ferrite with Zn^{2+} ions occupying tetrahedral A site with antiferromagnetic nature below Neel temperature 10.5 K and superparamagnetic nature at room temperature [10]. It is reported that compared to bulk ZnFe_2O_4 spinel ferrite, the nanoferrites have a significant proportion of Zn^{2+} distributed in the octahedral B site and also significant difference in lattice parameter with different cation distribution [11, 12].

The dependence of particle size on the magnetic behavior, i.e., ferromagnetic to super paramagnetic behavior by microwave-assisted hydrothermal synthesized ZnFe_2O_4 is reported by Anukorn Phuruangrat et al. [13]. The micro- to nanometric scale ferromagnetism in ZnFe_2O_4 is also reported to have mixed spinel state $(\text{Zn}_{1-x}\text{Fe}_x)^{\text{A}}[\text{Fe}_{2-x}\text{Zn}_x]^{\text{B}}$, where

Zn^{2+} and Fe^{3+} cations are distributed both in the tetrahedral (A) and octahedral (B) sites [14]. The variation of optical bandgap from 1.88 to 2.35 eV in $\text{Mn}_{1-x}\text{Zn}_x\text{Fe}_2\text{O}_4$ is reported by Hema et al. [15]. There are so many reports on (Ni, Mg, Cu, Co)-doped ZnFe_2O_4 , their cation distribution analysis, optical, photocatalytic, and magnetic properties [16–19].

There are only few reports on (Ca and Al) and the role of non-magnetic dopants (Ca and Mg) in GdFe_2O_4 and its different synthetic methods of preparation and structural, morphological, and magnetic properties [20, 21]. Zinc substituted CaFe_2O_4 powder prepared by hydrothermal method and a partially inverse spinel structure with Zn^{2+} occupying A site and the distribution of B site by Ca^{2+} and Fe^{3+} is reported by Abbas Kheradmand et al. [22]. There are hardly very few reports relevant to calcium-doped ZnFe_2O_4 available in the literature. It is found from the literature that none of the articles reveals the complete structural parameters, electronic charge density distribution and magnetic properties of Ca^{2+} -doped ZnFe_2O_4 spinel ferrites.

Thus, in the present work, $\text{Ca}_x\text{Zn}_{1-x}\text{Fe}_2\text{O}_4$ with $x = 0.0, 0.2, 0.4, 0.6$ was synthesized using solvothermal method. The average structural information was extracted from X-ray diffraction data using Rietveld refinements. The cation distribution analysis was carried out to understand the site occupancies in both tetragonal A site and octahedral B site, ionic radii of both A and B site, and the interaction between them. The electron density distribution and bonding nature of the samples were analyzed using the maximum entropy method (MEM). The surface morphology and elemental composition of the sample were identified using SEM/EDX. The optical bandgap and magnetic hysteresis properties were analyzed using UV–Vis spectrometer and vibrating sample magnetometer (VSM), respectively.

2 Experimental details

2.1 Sample preparation

A simple low-cost and low-temperature solvothermal technique was used for the synthesis of Ca^{2+} -doped ZnFe_2O_4 , because this method has its own advantages like precise control of the size, shape distribution and crystallinity of the product by adjusting

reaction temperature and type of solvents and surfactants, etc. [23]. The powder samples of $\text{Ca}_x\text{Zn}_{1-x}\text{Fe}_2\text{O}_4$ with $x = 0.0, 0.2, 0.4, 0.6$ were prepared using the stoichiometric ratio of AQanalar grade starting materials $\text{Fe}(\text{NO}_3)_3 \cdot 9\text{H}_2\text{O}$, $\text{Ca}(\text{NO}_3)_2 \cdot 4\text{H}_2\text{O}$, $\text{Zn}(\text{NO}_3)_2 \cdot 6\text{H}_2\text{O}$, ethylene glycol, sodium hydroxide and hydrochloric acid, purchased from Sigma-Aldrich, India, using the methodology followed by Abbas Kheradmand et al. [22].

2.2 Characterization techniques

Precise powder X-ray diffraction data were collected at room temperature with scanning angle 2θ from 10° to 120° in steps of nearly 0.02° using Bruker AXS D8 advance XRD instrument, with Cu-K_α X-ray radiation of wavelength $\lambda = 1.5406 \text{ \AA}$. The surface morphology and elemental composition of the samples ZnFe_2O_4 and $\text{Ca}_{0.2}\text{Zn}_{0.8}\text{Fe}_2\text{O}_4$ were analyzed using SEM/EDX instrument Jeol 6390LA/OXFORD XMX N with the accelerating voltage of 0.5 to 30 kV and the remaining samples, $\text{Ca}_{0.4}\text{Zn}_{0.6}\text{Fe}_2\text{O}_4$ and $\text{Ca}_{0.6}\text{Zn}_{0.4}\text{Fe}_2\text{O}_4$ were analyzed using TESCAN VEGA3 SPH. The magnetic hysteresis analysis (M versus H), at room temperature was carried out using VSM, Lakeshore, USA, Model 7407, with maximum magnetic field 2.5 T and dynamic moment range from 10^{-6} to 10^3 emu. The UV-Vis spectroscopy based optical band gap of the samples were analyzed using JASCO V-630 UV-Visible spectrophotometer.

The average lattice parameters of the samples were analyzed using unit cell refinement by the software Unitcell [24]. The cation distribution analysis was done using Bertaut method [25]. The average structural parameters like cell parameter, Oxygen positional parameter and structure factor for various lattice planes were analyzed by Rietveld refinement strategy [26] using the software JANA 2006 [27]. The electron density distribution and nature of bonding were analyzed using the versatile mathematical tool called MEM, introduced by Gull [28]. The experimental charge density of various application-oriented materials has been successfully explained by Saravanan et al. [29] using the software package Dysnomia [30]. 3D and 2D visualization and numerical bond length versus charge density calculations were plotted using the software VESTA [31].

3 Results and discussion

3.1 X-ray diffraction analysis

Powder X-ray diffraction data of the samples $\text{Ca}_x\text{Zn}_{1-x}\text{Fe}_2\text{O}_4$ with $x = 0.0, 0.2, 0.4, 0.6$, collected at room temperature have been indexed by comparing the diffraction angle values of the standard bulk cubic spinel ZnFe_2O_4 (JCPDS file no. 22-1012) [32]. Small amount of $\epsilon\text{-Fe}_2\text{O}_3$ (JCPDS file no. 16-0653) as an additional phase is found in the sample ZnFe_2O_4 . The peaks present in the sample (202), (311), (222), (400), (422), (511) and (440) confirms the cubic spinel formation with space group F_{d-3m} . Figure 1 presents peak shift analysis based on X-ray diffraction intensity data for all the compositions of the prepared samples.

There is a small shift in 2θ value for all the peaks toward the higher angles for the composition ZnFe_2O_4 to $\text{Ca}_{0.4}\text{Zn}_{0.6}\text{Fe}_2\text{O}_4$. This is due to the doping of higher ionic radius dopant (ionic radius of $\text{Ca}^{2+} = 0.99 \text{ \AA}$) in lesser radii host atoms (ionic radius of $\text{Zn}^{2+} = 0.74 \text{ \AA}$). The sample with $\text{Ca}_{0.6}\text{Zn}_{0.4}\text{Fe}_2\text{O}_4$ has a small shift in 2θ toward the lower 2θ angle compared to $\text{Ca}_{0.4}\text{Zn}_{0.6}\text{Fe}_2\text{O}_4$, which may be due to a slight lattice disorder by the effect of doping [33].

The cell parameters of the samples were studied using unit cell refinement methodology considering the cubic spinel ferrite structure using the software Unitcell [24]. The observed and calculated Bragg angles (2θ) and inter planar distances (d) perfectly match each other. Williamson and Hall plot method with the following formula is used for the calculation of average crystallite size and lattice microstrain [34]

$$\beta \cos \theta = 4\eta \sin \theta + K\lambda/D, \quad (1)$$

where β is the full width at half maximum (FWHM), θ is the diffraction angle, λ is the wavelength of X-ray, D is the average crystallite size and η is a lattice strain. The plot of $4\sin\theta$ versus $\beta\cos\theta$ is a straight-line giving slope η and y intercept $K\lambda/D$, which is shown in Fig. 2. The estimated lattice parameter, average crystallite size and lattice micro-strain are given in Table 1. It is found that the lattice parameter slightly increases linearly as the doping concentration increases. The minimum and maximum crystallite size is found to be nearly, 13 nm and 66 nm for the composition $\text{Ca}_{0.4}\text{Zn}_{0.6}\text{Fe}_2\text{O}_4$ and $\text{Ca}_{0.6}\text{Zn}_{0.4}\text{Fe}_2\text{O}_4$, respectively. The minimum and maximum lattice distortion will be 2.18×10^{-3} and 5.37×10^{-3} for the

Fig. 1 Peak shift analysis (2θ versus X-ray intensity)

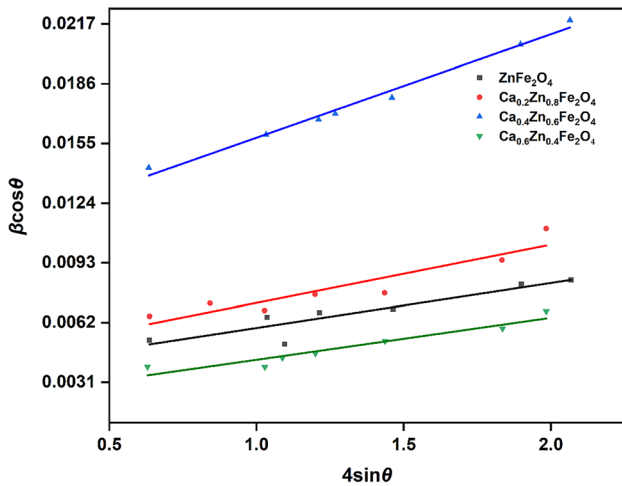
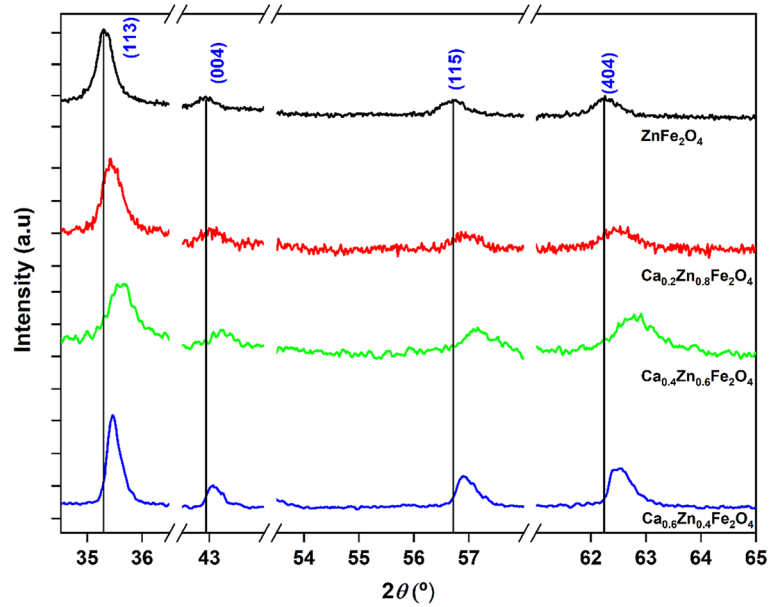


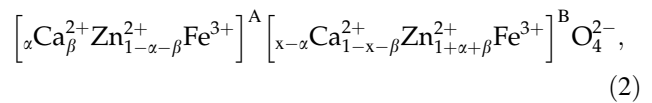
Fig. 2 Williamson–Hall plot

Table 1 Parameters refined using unit cell and Williamson–Hall plot

Sample name	Lattice parameter (Å)	Crystallite size (nm)	Lattice strain (10^{-3})
ZnFe ₂ O ₄	8.4396 (3)	38	2.83
Ca _{0.2} Zn _{0.8} Fe ₂ O ₄	8.4436 (1)	32	3.03
Ca _{0.4} Zn _{0.6} Fe ₂ O ₄	8.4471 (6)	13	5.37
Ca _{0.6} Zn _{0.4} Fe ₂ O ₄	8.4507 (1)	66	2.18

composition Ca_{0.6}Zn_{0.4}Fe₂O₄ and Ca_{0.4}Zn_{0.6}Fe₂O₄, respectively.

The distribution of the cations in the cubic spinel structure was carried out with the following assumption:



where α and β represents the occupancy of Ca²⁺ and Zn²⁺ in A site, respectively, with the conditions that the maximum occupancy in A site and B site is 1 and 2, respectively. The distributed cations in tetrahedral A and octahedral B site was calculated based on the intensity calculations [35]

$$I_{hkl} = |F_{hkl}|^2 P_{hkl} L_p, \quad (3)$$

where I_{hkl} is the relative integrated intensity of the particular lattice plane (hkl), F_{hkl} is the structure factor, P_{hkl} is the multiplicity factor and L_p is Lorentz polarization factor. The presence of cations at tetra-

hedral A site and octahedral B site is reported to be highly sensitive to the intensity of planes (220), (440), and (400), (422) [35]. The X-ray intensity ratios I_{220}/I_{400} , I_{220}/I_{422} , I_{400}/I_{440} , and I_{400}/I_{422} were calculated for various cation combinations which closely match with observed intensity ratio. Table 2 gives the parameters and results of cation distribution analysis

Table 2 Results of cation distribution analysis

Sample name	Cation active intensity ratios				Tetrahedral A site occupancy	Octahedral B site occupancy	Type of ferrite
	I_{400}/I_{440}		I_{220}/I_{422}				
	Cal	Obs	Cal	Obs			
ZnFe ₂ O ₄	0.634	0.617	3.563	4.975	(Zn _{1.0}) ^A	(Fe _{2.0}) ^B	Normal ferrite
Ca _{0.2} Zn _{0.8} Fe ₂ O ₄	0.639	0.635	3.599	3.6323	(Zn _{0.8} Ca _{0.046} Fe _{0.154}) ^A	(Ca _{0.154} Fe _{1.846}) ^B	Mixed ferrite
Ca _{0.4} Zn _{0.6} Fe ₂ O ₄	0.694	0.631	3.532	2.873	(Zn _{0.6} Ca _{0.145} Fe _{0.255}) ^A	(Ca _{0.255} Fe _{1.745}) ^B	Mixed ferrite
Ca _{0.6} Zn _{0.4} Fe ₂ O ₄	0.703	0.706	3.579	1.547	(Zn _{0.4} Ca _{0.44} Fe _{0.16}) ^A	(Ca _{0.16} Fe _{1.84}) ^B	Mixed ferrite

for all compositions of Ca_xZn_{1-x}Fe₂O₄ with x = 0.0, 0.2, 0.4, 0.6. The cation distribution results showed that Zn²⁺ always occupies in the tetrahedral A site and Ca²⁺ and Fe³⁺ shares both A and B sites, forming a mixed ferrite.

The Oxygen occupational parameter, hopping lengths and site radius of both tetrahedral A site and octahedral B site, bond length and bond angles were calculated [36, 37] and tabulated in Table 3.

The hopping length L_A and L_B increases as the Ca²⁺ content increases and L_A is greater than L_B as reported earlier [38]. The distance between the magnetic ions increases as the doping of Ca²⁺ content increases. This is because of the difference in ionic radii of the ions, Ca²⁺ (0.99 Å) and Zn²⁺ (0.74 Å). Hence, the distance between the magnetic ions increases as the Ca²⁺ content increases. Also, it is seen from the Table 3 that the radius of the tetrahedral sites are

Table 3 Parameters refined using Rietveld refinement and cation distribution analysis

Parameters	ZnFe ₂ O ₄	Ca _{0.2} Zn _{0.8} Fe ₂ O ₄	Ca _{0.4} Zn _{0.6} Fe ₂ O ₄	Ca _{0.6} Zn _{0.4} Fe ₂ O ₄
Lattice parameter (a) (Å)	8.4412 (2)	8.4438 (1)	8.4466 (5)	8.4502 (3)
X-ray density (g/cm ³)	5.3242	5.2077	5.0901	4.9729
Unit cell electrons, F ₍₀₀₀₎	912.00	896.00	880	864
wRp (%)	2.64	2.92	6.79	7.69
Hopping length (L _A) (Å)	3.6551	3.6562	3.6575	3.6590
Hopping length (L _B) (Å)	2.9844	2.9853	2.9863	2.9876
U ^{43m}	0.38117	0.38106	0.37874	0.37836
U ^{3m}	0.2562	0.25611	0.22380	0.2534
R _{A(exp)} (Å)	0.57779	0.57673	0.54345	0.5387
R _{B(exp)} (Å)	0.71820	0.71979	0.74006	0.74415
Inter-ionic distances (Me–Me) (Å)	b = 2.9844	2.98533	2.98632	2.98760
	c = 3.4995	3.50061	3.50178	3.50327
	d = 3.6551	3.65627	3.65749	3.65904
	e = 5.4827	5.48441	5.48623	5.48857
	f = 5.1692	5.17075	5.17247	5.17467
Inter-ionic distances (Me–O) (Å)	p = 2.0577	2.05935	2.07989	2.08402
	q = 1.9186	1.91752	1.88375	1.87895
	r = 3.6738	3.67177	3.60710	3.59791
	s = 3.6854	3.68607	3.67582	3.67552
Bond angles (°)	θ ₁ = 123.267	123.322	124.054	124.176
	θ ₂ = 144.627	144.864	148.266	148.867
	θ ₃ = 92.9656	92.8822	91.7632	91.5799
	θ ₄ = 125.942	125.924	125.672	125.630
	θ ₅ = 74.2854	74.4306	76.4565	76.8028

greater than octahedral sites and the tetrahedral A site radius gradually decreases and octahedral B site radius increases, as the Ca^{2+} doping concentration is increased for the compositions of $\text{Ca}_x\text{Zn}_{1-x}\text{Fe}_2\text{O}_4$ from $x = (0.0 \text{ to } 0.6)$ and the numerical results are consistent with reported one for ZnFe_2O_4 [38]. There is an increase in trend of Me–Me and Me–O interionic distances except q, r, s , which indeed decreases with increase in doping concentration. The bond angles $\theta_1, \theta_2, \theta_5$ increases where as θ_3 and θ_4 decreases with respect to increase in dopant concentration.

3.2 Rietveld analysis

Precisely collected powder X-ray diffraction data of all the samples of $\text{Ca}_x\text{Zn}_{1-x}\text{Fe}_2\text{O}_4$ are refined using the JANA2006 software [27] adopting Rietveld refinement technique [26]. The structural refinement process include cell refinement, Pseudo-voigt as peak shape function, Berar–Baldinazzi as asymmetry correction, March Dollase as preferred orientation and Legendre polynomials as background function along with anion (oxygen) occupational positions. The initial fractional coordinators were fixed as (0 0 0), (0.625, 0.625, 0.625) and (0.375, 0.375, 0.375) for tetrahedral A site, octahedral B site and oxygen occupancy, respectively. Figure 3a–d represents the refined JANA profile along with Bragg positions and the difference between observed and calculated intensities for all the samples. All JANA fitted profile show the perfect fitting of all cubic spinel peaks corresponding to the space group F_{d-3m} , with very little error and without any impurity phase, except for the sample ZnFe_2O_4 .

The refined structural parameters based on Rietveld refinement are also reported in Table 3. A decrease in $F_{(000)}$, number of electrons present in the unit cell, with respect to increase in doping concentration is yet another confirmation of doping of lesser charged (atomic number) Ca^{2+} in higher charged (atomic number) Zn^{2+} in $\text{Ca}_x\text{Zn}_{1-x}\text{Fe}_2\text{O}_4$. The weighted profile R factor wRp is very small, which explains how well the data are fitted with the model and also the quality of the experimental XRD data.

Figure 4 presents the variation of cell parameter and X-ray density with respect to doping concentration. It is found that cell parameter increases and X-ray density decreases linearly with doping concentration. The linear increase in cell parameter with doping concentration, showing little expansion of the

unit cell may be due to replacement of smaller Zn^{2+} ions 0.74 Å by larger Ca^{2+} ions 0.99 Å. This linear change in cell parameter with doping concentration is usual in solid solutions of soft ferrites [39].

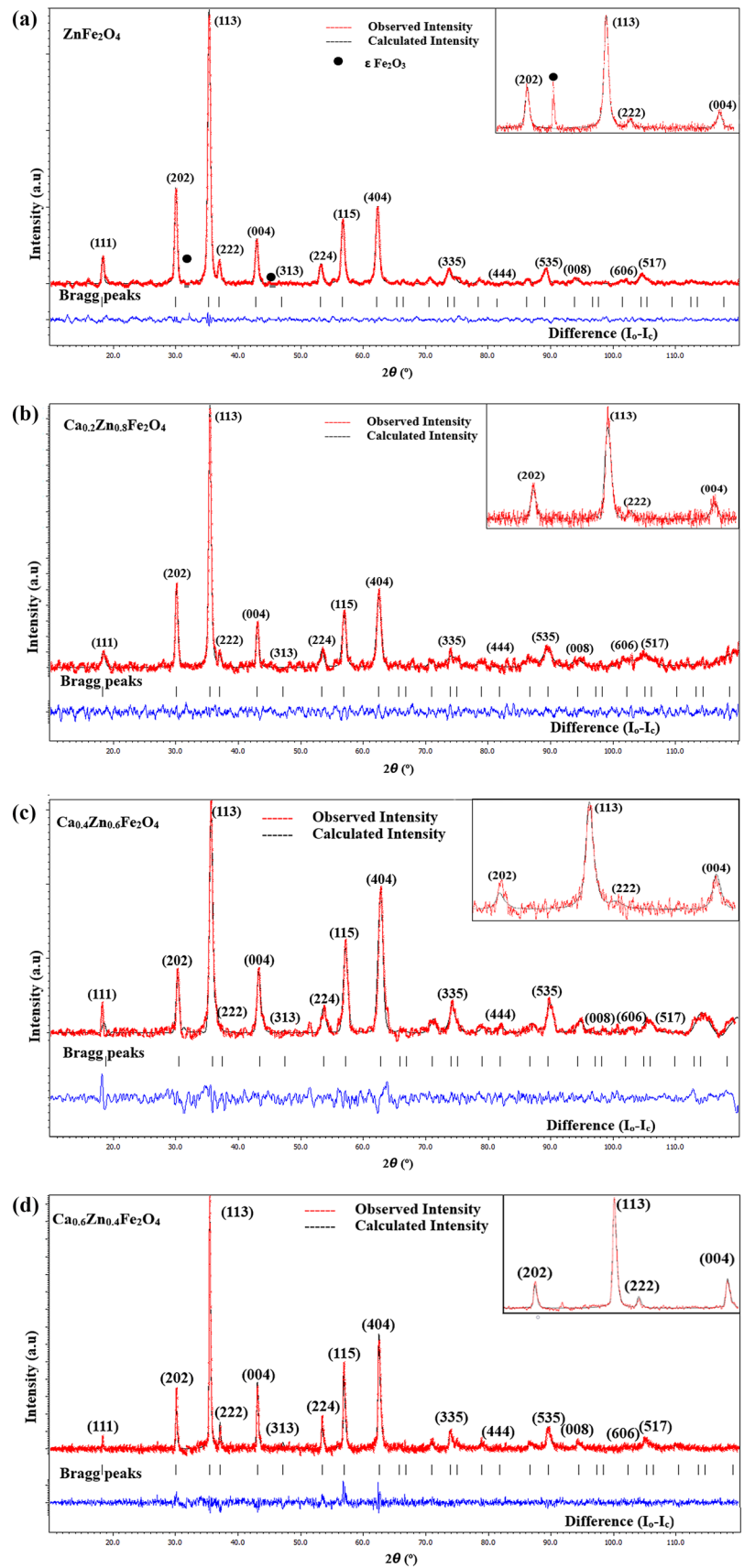
3.3 Electron density analysis by MEM

The precise charge density distribution inside the unit cell for the prepared samples is calculated from the structure factor, extracted using the X-ray diffraction data by Rietveld refinement method. The electronic charge density is calculated using the entropy calculations by a mathematical tool, MEM, initially fixing the prior uniform charge density (F_{000}/a^3) inside the entire unit cell. The unit cell is divided into $(108 \times 108 \times 108)$ pixels along three axis a, b, c (lattice parameters) and the entropy calculations are carried out in each pixel using the software package *Dysnomia* [30]. The visual presentation of the electron density in 3D, 2D and 1D is plotted by the software package *VESTA* [31]. Three-dimensional electron density of $\text{Ca}_x\text{Zn}_{1-x}\text{Fe}_2\text{O}_4$ with $x = 0.0, 0.2, 0.4, 0.6$, with unit cell boundary 0.5 to 1.0 along the c axis in the isosurface level $1.0 \text{ e}/\text{Å}^3$ is shown in Fig. 5a–d.

The alternative tetrahedral A site and octahedral B site is clearly visible, which confirms the cubic spinel ferrite formation. The covalent bond domination can be visualized in A site with elongated A–O bonding and is maximum for the composition $x = 0.2$ and ionic bond domination can be visualized in the B site with more spherical localized electron cloud around B site and is maximum for the composition $\text{Ca}_{0.2}\text{Zn}_{0.8}\text{Fe}_2\text{O}_4$. It is found that the B–B interaction for the composition $\text{Ca}_{0.2}\text{Zn}_{0.8}\text{Fe}_2\text{O}_4$ seems to be purely ionic with maximum localization of spherical charges and gradual increase in elongation all other cases which is maximum for the composition $\text{Ca}_{0.6}\text{Zn}_{0.4}\text{Fe}_2\text{O}_4$.

The two-dimensional electronic charge density distribution on the miller plane (110) of all the samples in the electron density range of $0.02 \text{ e}/\text{Å}^3$ to $2.0 \text{ e}/\text{Å}^3$ with contour interval level of $0.15 \text{ e}/\text{Å}^3$ is given in Fig. 6a–d. Localized and spherical nature of the electronic charge density distribution around B site shows pure ionic nature with O site and is maximum (minimum bond density) for the composition $\text{Ca}_{0.2}\text{Zn}_{0.8}\text{Fe}_2\text{O}_4$. Non-spherical and stretching type charge density distribution of A site and O site shows pure Covalent nature in 2D and is maximum for the composition $\text{Ca}_{0.2}\text{Zn}_{0.8}\text{Fe}_2\text{O}_4$.

Fig. 3 **a** Rietveld refined X-ray profile of ZnFe_2O_4 using JANA2006. **b** Rietveld refined X-ray profile of $\text{Ca}_{0.2}\text{Zn}_{0.8}\text{Fe}_2\text{O}_4$ using JANA2006. **c** Rietveld refined X-ray profile of $\text{Ca}_{0.4}\text{Zn}_{0.6}\text{Fe}_2\text{O}_4$ using JANA2006. **d** Rietveld refined X-ray profile of $\text{Ca}_{0.6}\text{Zn}_{0.4}\text{Fe}_2\text{O}_4$ using JANA2006



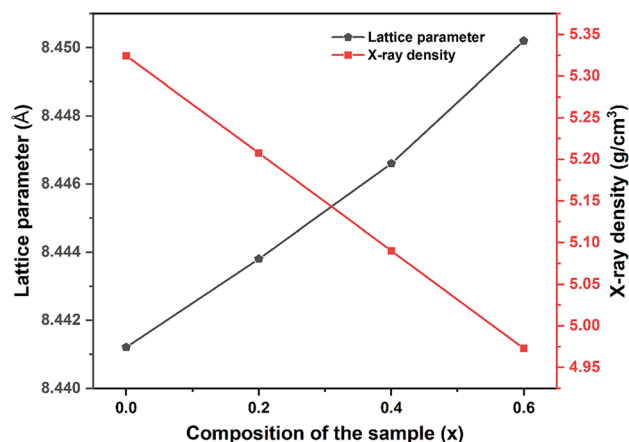


Fig. 4 Variation of lattice parameter and X-ray density with doping concentration

The 1D charge density interactions between tetrahedral A, octahedral B and Oxygen ions for all the compositions are given in Fig. 7a–e and the numerical mid bond electron density with bond length distribution is given in Table 4. Normally in ferrites, among the three interactions, A–B interaction is the strongest and A–A interaction is the weakest [36]. The same nature is also revealed in MEM 1D results, as reported.

Though A–B interaction is strongest among the three interactions, the numerical value of the electron density ($0.4728 \text{ e}/\text{Å}^3$) is small leading to non-collinear spin order between A and B site. It is found from both Fig. 7 and Table 4 that A–A mid bond electron density gradually increases to a maximum at $\text{Ca}_{0.2}\text{Zn}_{0.8}\text{Fe}_2\text{O}_4$, which is $0.0841 \text{ e}/\text{Å}^3$, then decreases and bond length gradually decreases up to the composition $\text{Ca}_{0.4}\text{Zn}_{0.6}\text{Fe}_2\text{O}_4$, then slightly increases. B–B mid bond electron density shows ionic bonding nature and minimum mid bond density for the composition $\text{Ca}_{0.2}\text{Zn}_{0.8}\text{Fe}_2\text{O}_4$, which is $0.1339 \text{ e}/\text{Å}^3$ and its bond length is also maximum. A–B mid bond electron density shows increasing trend up to the composition $\text{Ca}_{0.2}\text{Zn}_{0.8}\text{Fe}_2\text{O}_4$, which has a maximum value $0.4728 \text{ e}/\text{Å}^3$ and then decreases and shows ionic bonding nature. Also, its bond length increases up to $\text{Ca}_{0.4}\text{Zn}_{0.6}\text{Fe}_2\text{O}_4$ and then decreases. A–O mid bond electron density increases to a maximum at $\text{Ca}_{0.2}\text{Zn}_{0.8}\text{Fe}_2\text{O}_4$, which is $1.4452 \text{ e}/\text{Å}^3$ and then decreases, shows strong covalent bonding nature and its bond length shows a decreasing trend showing the shrinkage of tetrahedral site (which is also evident from tetrahedral radius which decreases with

increase of doping). B–O mid bond electron density decreases up to the composition $\text{Ca}_{0.2}\text{Zn}_{0.8}\text{Fe}_2\text{O}_4$, which is $0.49 \text{ e}/\text{Å}^3$ with slight random increase thereafter and also show pure ionic character. B–O bond length shows an increasing trend showing the expansion of octahedral site (which is also evident from octahedral radius R_B which increases with increase of doping). It is also found from 1D diagrams that A–A, A–B, A–O mid bond electron density values are maximum for the composition $x = 0.2$ and B–B, B–O mid bond electron density values are minimum for the composition $\text{Ca}_{0.2}\text{Zn}_{0.8}\text{Fe}_2\text{O}_4$.

3.4 Magnetic hysteresis analysis

Figure 8 presents the M – H curve using vibration sample magnetometer (VSM) for all the grown samples at room temperature, with inset showing (a) coercivity (H_{ci}) and remanence (M_r) for ZnFe_2O_4 and $\text{Ca}_{0.2}\text{Zn}_{0.8}\text{Fe}_2\text{O}_4$, (b) coercivity (H_{ci}) and remanence (M_r) for $\text{Ca}_{0.4}\text{Zn}_{0.6}\text{Fe}_2\text{O}_4$, and $\text{Ca}_{0.6}\text{Zn}_{0.4}\text{Fe}_2\text{O}_4$, and (c) saturation magnetization (M_s) for all the samples.

Table 5 gives the VSM analyzed magnetic parameters, which reveals that all compositions are ferromagnetic in nature and comes under the category of semi-hard ferrites. The saturation magnetization (M_s) is almost same for all the compositions ranging from 31.103 to 36.355 emu/g. But the remanent magnetization (M_r) and coercivity (H_{ci}) have the maximum values 9.4265 emu/g, 10.372 emu/g and 407.98 G, 404.27 G for the samples $\text{Ca}_{0.2}\text{Zn}_{0.8}\text{Fe}_2\text{O}_4$ and $\text{Ca}_{0.4}\text{Zn}_{0.6}\text{Fe}_2\text{O}_4$, respectively.

The variation of M_s and M_r versus crystallite size shown in Fig. 9 shows an optimum M_s and M_r values at crystallite size nearly 33 nm.

The variation of H_{ci} and squareness ratio (M_r/M_s) shown in Fig. 10 also shows optimum and maximum values for the crystallite size nearly 33 nm, corresponding to the composition of the sample $\text{Ca}_{0.2}\text{Zn}_{0.8}\text{Fe}_2\text{O}_4$. The Bohr magnetron (μ_B^H), i.e., magnetic moment per formula unit is calculated from saturation magnetization M_s value, using Eq. (4) [40].

$$\mu_B^H = \left\{ \frac{\text{Molecular weight}}{5585} \right\} \times M_s \quad (4)$$

The value of Bohr magnetron calculated based on cation distribution and Neel's two sublattice model of ferromagnetism, using the relation $\mu_B^N = M_B - M_A$ (where M_B and M_A are sublattice magnetization) is

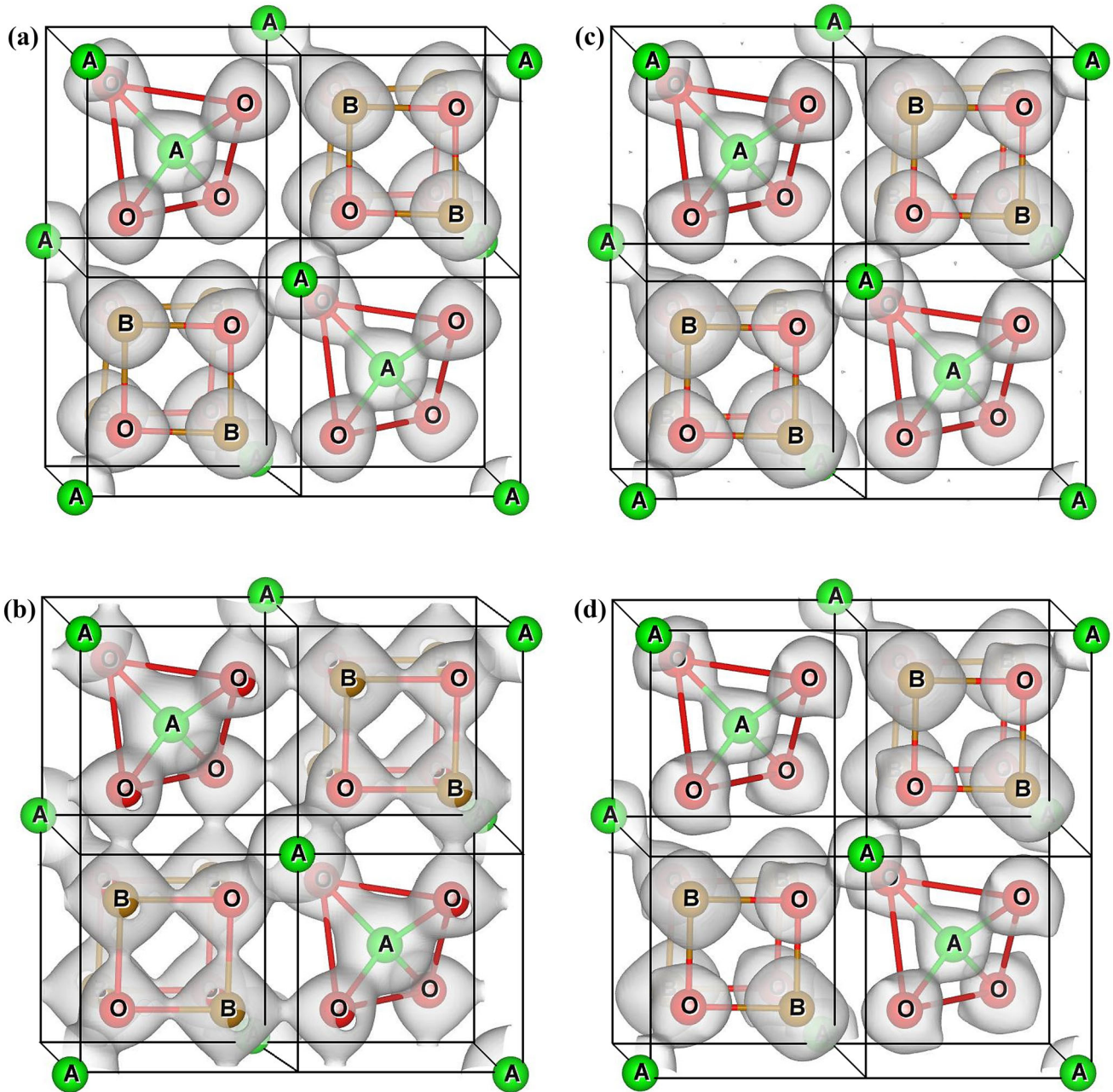


Fig. 5 **a** 3D MEM electron density distribution of ZnFe_2O_4 (unit cell boundary 0.5 to 1.0 along c axis, isosurface level $1.0 \text{ e}/\text{\AA}^3$). **b** 3D MEM electron density distribution of $\text{Ca}_{0.2}\text{Zn}_{0.8}\text{Fe}_2\text{O}_4$ (unit cell boundary 0.5 to 1.0 along c axis, isosurface level $1.0 \text{ e}/\text{\AA}^3$).

c 3D MEM electron density distribution of $\text{Ca}_{0.4}\text{Zn}_{0.6}\text{Fe}_2\text{O}_4$ (unit cell boundary 0.5 to 1.0 along c axis, isosurface level $1.0 \text{ e}/\text{\AA}^3$). **d** 3D MEM electron density distribution of $\text{Ca}_{0.6}\text{Zn}_{0.4}\text{Fe}_2\text{O}_4$ (unit cell boundary 0.5 to 1.0 along c axis, isosurface level $1.0 \text{ e}/\text{\AA}^3$).

given in Table 5. There is a difference in μ_B^H and μ_B^N , due to the non-collinear spin ordering in the samples. This non-collinear spin ordering is due to the presence of Yafet–Kittel (YK) angle (α_{yk}), which is calculated using the relation (5) is given in Table 5.

$$\mu_B^H = M_B \cos \alpha_{yk} - M_A. \quad (5)$$

3.5 SEM/EDX analysis

Scanning electron microscopy (SEM) and Energy dispersive spectrum (EDX) analysis is carried out to study the surface morphology and elemental composition of all the prepared samples. The SEM images

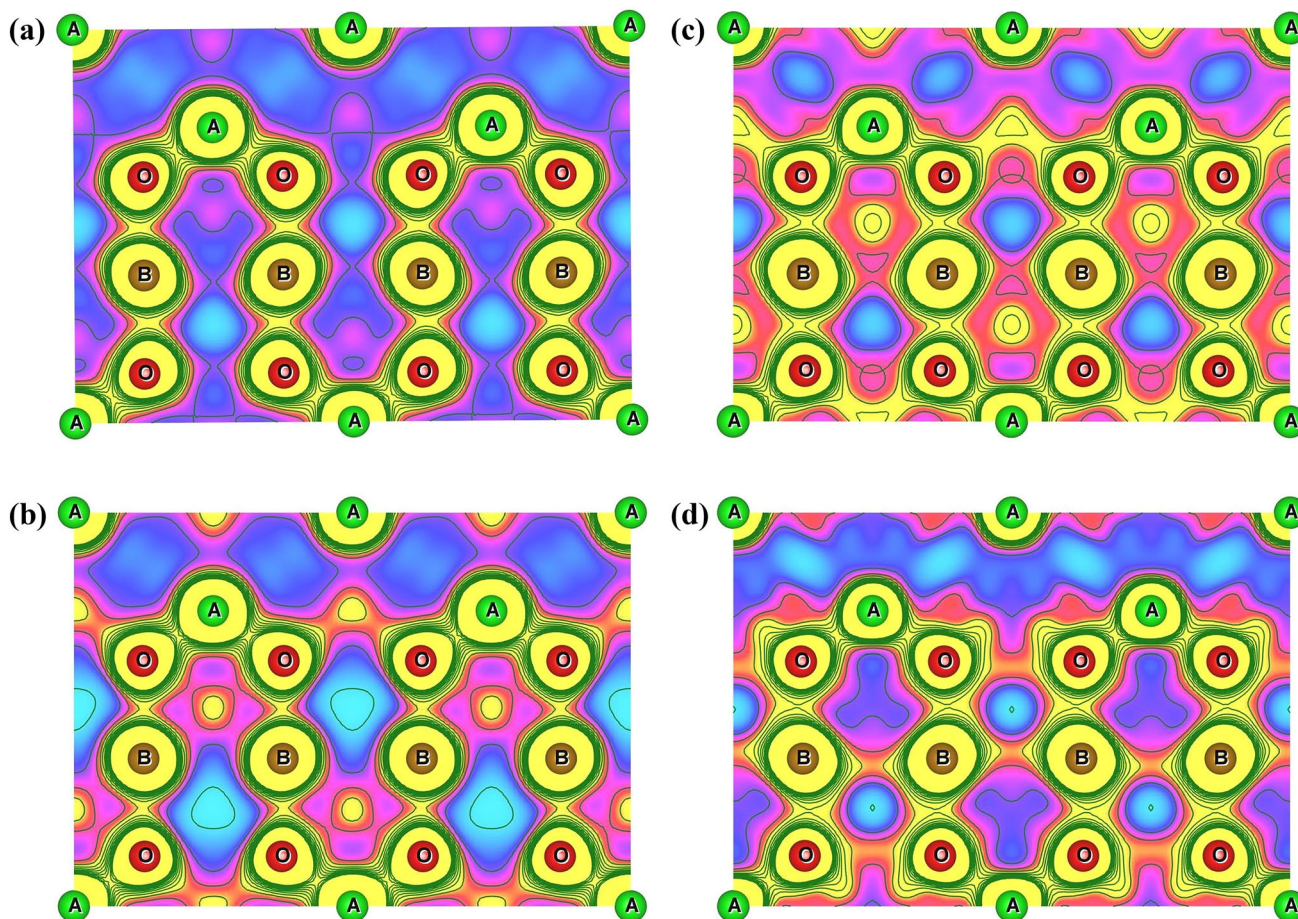


Fig. 6 **a** 2D MEM electron density of ZnFe_2O_4 on the miller plane (110). (Contour range $0.02 \text{ e}/\text{\AA}^3$ to $2.0 \text{ e}/\text{\AA}^3$ with interval $0.15 \text{ e}/\text{\AA}^3$). **b** 2D MEM electron density of $\text{Ca}_{0.2}\text{Zn}_{0.8}\text{Fe}_2\text{O}_4$ on the miller plane (110) (Contour range $0.02 \text{ e}/\text{\AA}^3$ to $2.0 \text{ e}/\text{\AA}^3$ with interval $0.15 \text{ e}/\text{\AA}^3$). **c** 2D MEM electron density of $\text{Ca}_{0.4}\text{Zn}_{0.6}\text{Fe}_2\text{O}_4$ on the

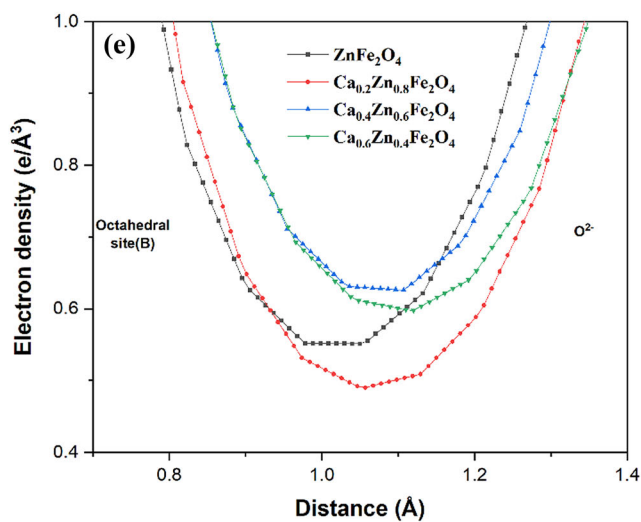
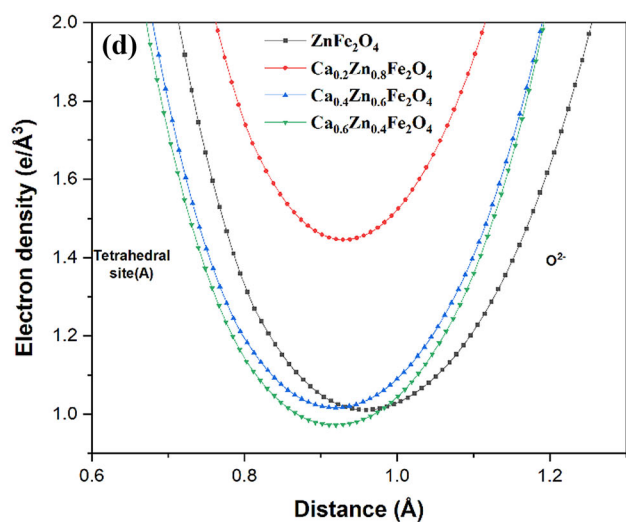
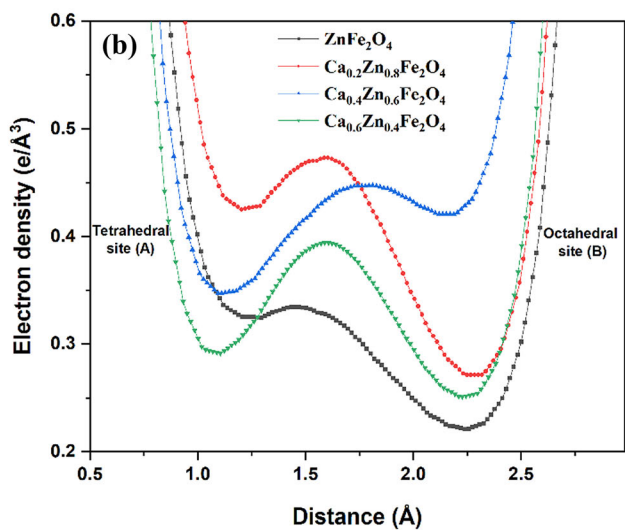
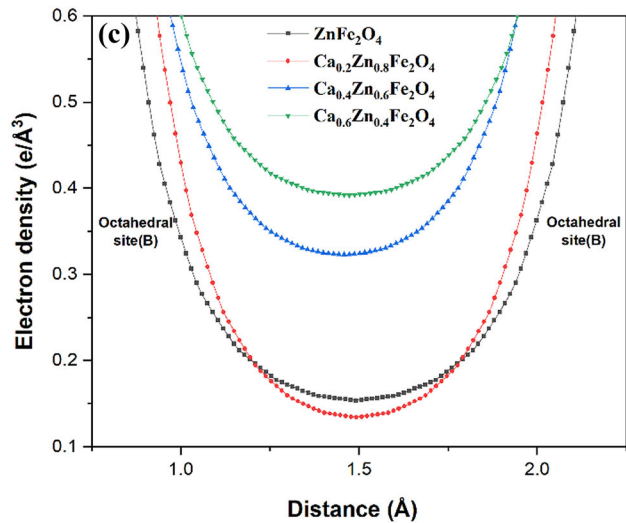
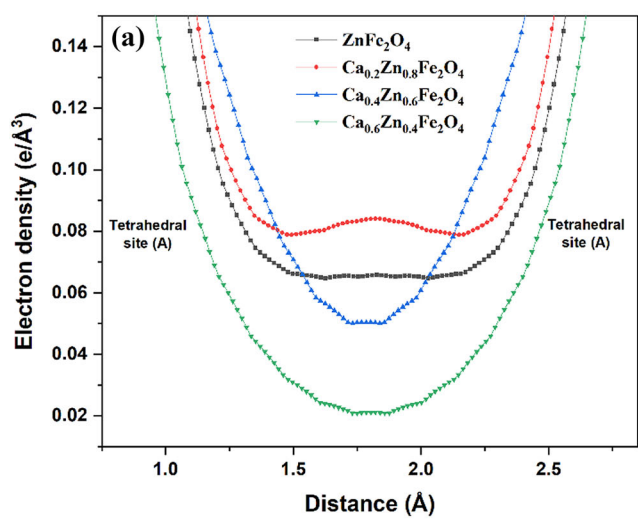
miller plane (110) (Contour range $0.02 \text{ e}/\text{\AA}^3$ to $2.0 \text{ e}/\text{\AA}^3$ with interval $0.15 \text{ e}/\text{\AA}^3$). **d** 2D MEM electron density of $\text{Ca}_{0.6}\text{Zn}_{0.4}\text{Fe}_2\text{O}_4$ on the miller plane (110) (Contour range $0.02 \text{ e}/\text{\AA}^3$ to $2.0 \text{ e}/\text{\AA}^3$ with interval $0.15 \text{ e}/\text{\AA}^3$)

of the prepared samples with different magnification from 7.5 to 69 K with accelerating potential of 20 kV were observed. Figure 11a–d presents the EDX elemental composition along with the inset, the SEM image, for all the compositions of the prepared samples. Spherical particle nature and homogeneous distribution of particle with well-defined grain boundary are revealed in all the prepared samples with average particle size ranging from 500 to 900 nm. A very small percentage of agglomeration is also found in all the prepared samples. The EDX image of all the prepared compositions show the trace of the constituent elemental compositions like Ca, Zn, Fe and O. There is no trace of other elements found in the sample, shows the purity of the prepared samples. The gradual decrease in concentration of Zn^{2+} composition with the increase in doping

of Ca^{2+} is clearly visible in the EDX graph, showing the expected doping, qualitatively. It is found from the inset of Fig. 11a that there is a rod-like structure only in the sample ZnFe_2O_4 which may be due the presence of $\epsilon\text{-Fe}_2\text{O}_3$ [41]. Perfect spherical nature of the nanosized particles is found in all the samples except $\text{Ca}_{0.6}\text{Zn}_{0.4}\text{Fe}_2\text{O}_4$.

3.6 UV-Visible spectrophotometry

The UV-Vis spectrophotometry is a quantitative determination of optical bandgap from the discrete absorption or transmission of UV and visible light wavelength by the sample constituents inside the solution in comparison with the reference solvent. The ultraviolet part of the spectrum is obtained by a deuterium lamp and visible part by Tungsten



◀**Fig. 7** **a** 1D MEM electron density mapping (tetrahedral A–tetrahedral A interactions). **b** 1D MEM electron density mapping (tetrahedral A–octahedral B interactions). **c** 1D MEM electron density mapping (octahedral B–octahedral B interactions). **d** 1D MEM electron density mapping (tetrahedral A–O²⁻ interactions). **e** 1D MEM electron density mapping (octahedral B–O²⁻ interactions)

filament lamp. The absorption data were taken from 200 to 800 nm in steps of 0.2 nm. The switching between two different light sources in a single measurement occurs at 340 nm. Figure 12 presents the optical bandgap of the samples, calculated by Tauc plot with energy in (eV) versus $(\alpha hv)^2$ in $(eV\text{ cm}^{-1})^2$. All the prepared compositions of the sample show

direct bandgap nature with bandgap energy from 2.622 to 2.923 eV. As the Ca²⁺ doping concentration increases the bandgap energy also gradually increases, which may be attributed due the increase in porosity as shown from SEM images [42] and localized nature of density of states as mentioned in two-dimensional MEM images.

4 Conclusion

All the compositions of Ca²⁺-doped ZnFe₂O₄ samples show mixed spinel structure, except ZnFe₂O₄, which is normal spinel ferrite structure and mixed bonding nature, both covalent and ionic bonding. Tetrahedral A site is dominated with covalent bonding and

Table 4 Results of MEM refined 1D electron density distribution

Sample name	ZnFe ₂ O ₄		Ca _{0.2} Zn _{0.8} Fe ₂ O ₄		Ca _{0.4} Zn _{0.6} Fe ₂ O ₄		Ca _{0.6} Zn _{0.4} Fe ₂ O ₄	
	distance (Å)	Mid bond density (e/Å ³)	Distance (Å)	Mid bond density (e/Å ³)	Distance (Å)	Mid bond density (e/Å ³)	Distance (Å)	Mid bond density (e/Å ³)
A–A	1.8267	0.0658	1.8213	0.0841	1.7854	0.0505	1.8037	0.0211
B–B	1.4915	0.1535	1.4926	0.1339	1.4578	0.3227	1.4727	0.3917
A–B	1.4516	0.3344	1.5868	0.4728	1.7949	0.4472	1.6060	0.3942
A–O	0.9590	1.0109	0.9288	1.4452	0.9195	1.0166	0.9193	0.9723
B–O	1.0498	0.5505	1.0567	0.4900	1.1070	0.6261	1.1200	0.5976

Fig. 8 VSM—magnetic hysteresis with insets (a–c) showing its enlarged view

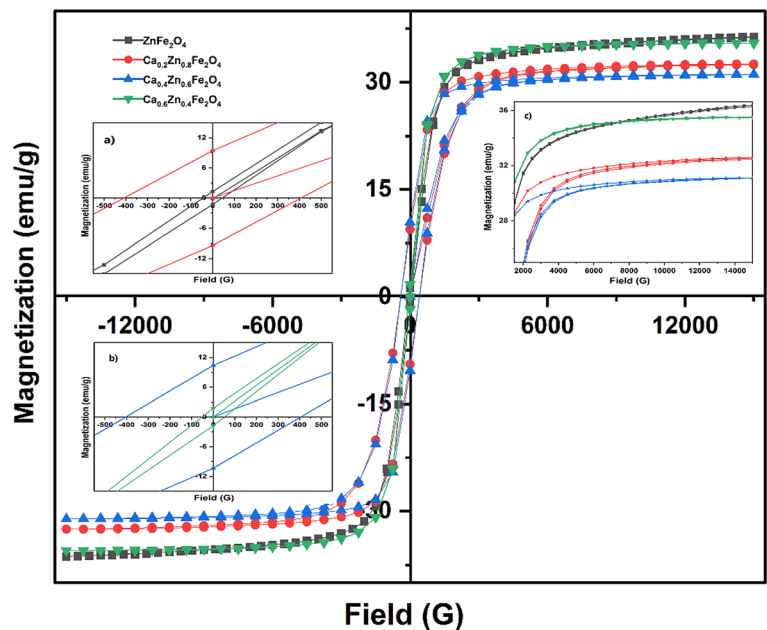


Table 5 Magnetic parameters obtained from VSM analysis

Parameters	ZnFe ₂ O ₄	Ca _{0.2} Zn _{0.8} Fe ₂ O ₄	Ca _{0.4} Zn _{0.6} Fe ₂ O ₄	Ca _{0.6} Zn _{0.4} Fe ₂ O ₄
M_s (emu/g)	36.355	32.558	31.103	35.527
M_r (emu/g)	1.2871	9.4265	10.372	1.7567
M_r/M_s	0.0354	0.2895	0.3335	0.0494
H_{ci} (G)	44.306	407.98	404.27	51.396
μ_B^H	1.5693	1.3759	1.2862	1.4369
μ_B^N	10	8.46	7.6	8.4
Yafet–Kittel angle (°)	80.97	76.55	73.95	75.92

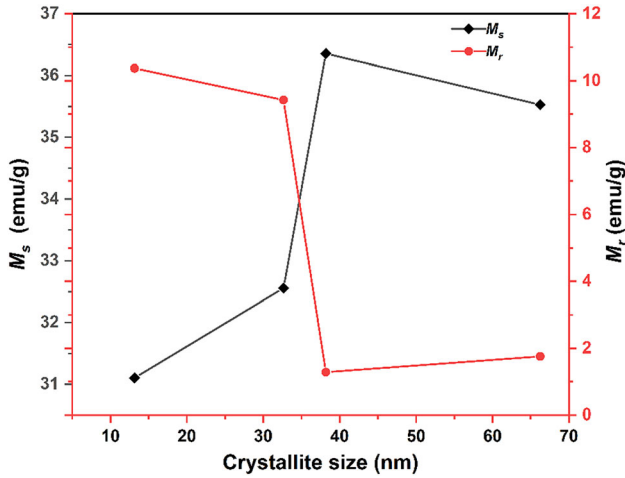


Fig. 9 Variation of M_s and M_r with crystallite size

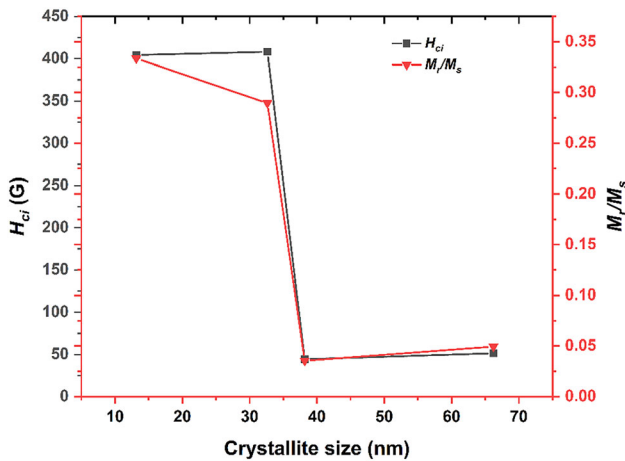


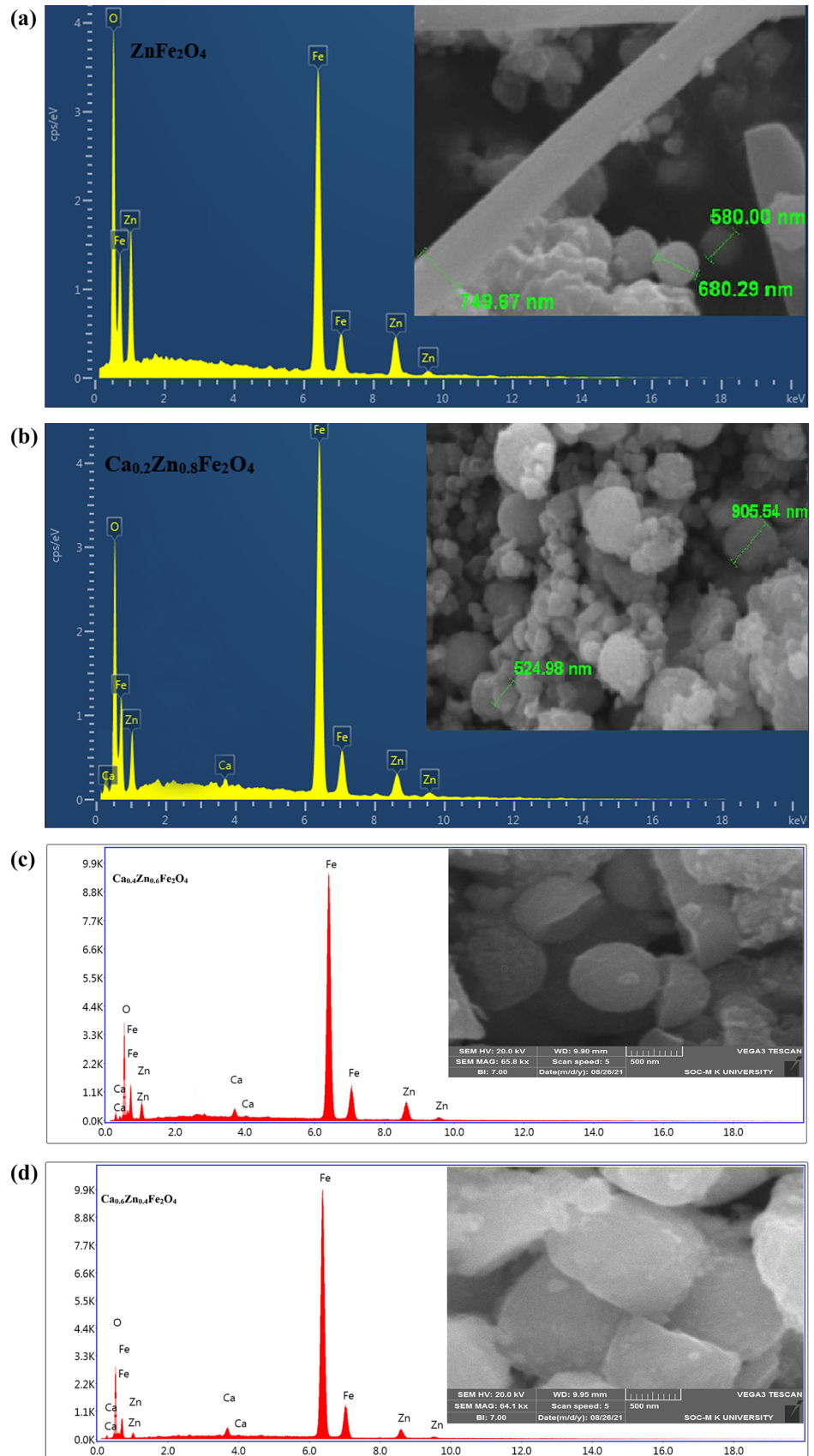
Fig. 10 Variation of H_{ci} and squareness ratio with crystallite size

octahedral B site is dominated with ionic bonding nature. The electron density analysis using MEM reveal that the A–B interaction is stronger than A–A and B–B interactions and A–A interaction is the weakest like other reported spinel ferrites. Experimental charge density studies reveal that the A–O site bonding has maximum bond density and covalent in nature and B–O site bonding is optimum with ionic nature for the composition Ca_{0.2}Zn_{0.8}Fe₂O₄. The SEM image of all the samples show perfect spherical particle nature. The EDX shows the presence of the elements Ca, Zn, Fe and O, without any impurity elements. The magnetic hysteresis shows optimum ferromagnetism for the composition Ca_{0.2}Zn_{0.8}Fe₂O₄. A non-collinear spin ordering between tetrahedral A site and octahedral B site is existing, which is explained by Yafet–Kittel angle. In conclusion, the magnetic studies along with the experimental charge density analysis, for the composition Ca_{0.2}Zn_{0.8}Fe₂O₄ show optimum magnetic properties, which may be used as an alternative low-cost semi-hard ferrite with further physical investigations.

5 Data transparency

The authors declare that all data supporting the findings of this study are available within the article and its supplementary information files.

Fig. 11 **a** EDX composition with inset the SEM micrograph for $ZnFe_2O_4$. **b** EDX composition with inset the SEM micrograph for $Ca_{0.2}Zn_{0.8}Fe_2O_4$. **c** EDX composition with inset the SEM micrograph for $Ca_{0.4}Zn_{0.6}Fe_2O_4$. **d** EDX composition with inset the SEM micrograph for $Ca_{0.6}Zn_{0.4}Fe_2O_4$



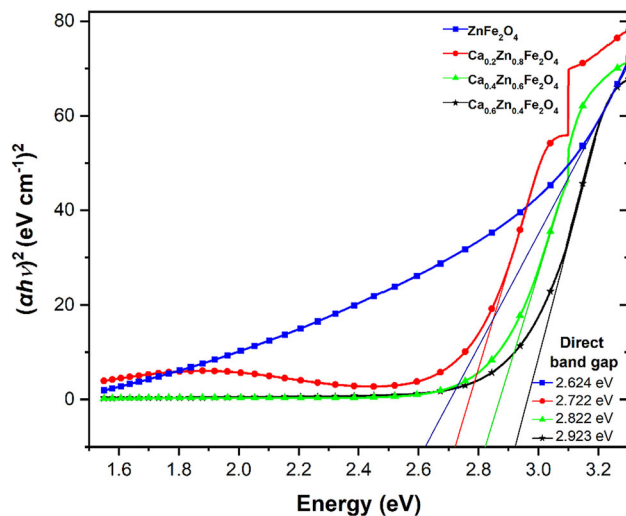


Fig. 12 Optical bandgap analysis using Tauc plot

Acknowledgements

The authors extend their heartfelt thanks to the Research Centre and PG department of Physics, Hajee Karutha Rowther Howdia College, Uthamapalayam 625 533, Tamil Nadu and Department of Physics, Sri Adi Chunchanagiri Women' College, Cumbum, 625 516, Tamil Nadu. The authors sincerely acknowledge SAIF (Sophisticated Analytical Instrument Facility), STIC, Cochin University, Cochin, Kerala for the powder XRD, SEM and EDX: Instrumental Facilities, CIC, Madurai Kamaraj University for SEM and EDAX, Department of Chemistry, Indian Institute of Technology, Chennai, for the VSM measurements and Department of Chemistry, Hajee Karutha Rowther Howdia College, Uthamapalayam 625 533, Tamil Nadu for UV-Vis spectrophotometry studies.

Author contributions

MT: Investigation, Formal analysis, writing original draft. MCR: Supervision, Conceptualization, Methodology. NP: Data Curation, Writing review and Editing. RS: Supervision, Software. YBK: Executing graphical techniques, Resources, SBP: Electronic artwork and Editing.

Funding

The authors did not receive support from any organization for the submitted work.

Declarations

Conflict of interest The authors declare that they have no known financial interests in any form or personal political and religious relationship that could have appeared to influence the work reported in this paper.

Supplementary Information: The online version contains supplementary material available at <http://doi.org/10.1007/s10854-021-07605-8>.

References

1. R. Masrour, H. El Moussaoui, E. Salmani, O. Mounkachi, H. Ez-Zahraouy, M. Hamedoun, E.K. Hlil, A. Benyoussef, J. Supercond. Nov. Magn. **27**, 177 (2013)
2. A. Veditnam, K. Kalauni, S. Dubey, A. Kumar, AIMS Mater. Sci. **7**, 800 (2020). <https://doi.org/10.3934/matersci.2020.6.800>
3. K. Praveena, K. Sadhana, S. Bharadwaj, S.R. Murthy, J. Magn. Mater. **321**, 2433 (2009). <https://doi.org/10.1016/j.jmmm.2009.02.138>
4. A.G. Olabi, A. Grunwald, Mater. Des. **29**, 469 (2008). <https://doi.org/10.1016/j.matdes.2006.12.016>
5. J. Wang, X. Gao, C. Yuan, J. Li, X. Bao, J. Magn. Mater. **401**, 662 (2016)
6. S.P. Gubin, Y.A. Koksharov, G.B. Khomutov, G.Y. Yurkov, Usp. Khim. **74**, 539 (2005). <https://doi.org/10.1070/RC2005v074n06ABEH000897>
7. P.B.C. Rao, S.P. Setty, Int. J. Eng. Sci. Technol. **2**, 3351 (2010)
8. Y.B. Kannan, R. Saravanan, N. Srinivasan, K. Praveena, K. Sadhana, J. Mater. Sci. Mater. Electron. **27**, 12000 (2016). <https://doi.org/10.1007/s10854-016-5347-y>
9. Y.B. Kannan, R. Saravanan, N. Srinivasan, K. Praveena, K. Sadhana, Phys. B Condens. Matter. **502**, 181 (2016). <https://doi.org/10.1016/j.physb.2016.09.006>
10. C. Yao, Q. Zeng, G.F. Goya, T. Torres, J. Liu, H. Wu, M. Ge, Y. Zeng, Y. Wang, J.Z. Jiang, J. Phys. Chem. C **111**, 12274 (2007). <https://doi.org/10.1021/jp0732763>
11. M. Dhiman, R. Sharma, V. Kumar, S. Singhal, Ceram. Int. **42**, 12594 (2016). <https://doi.org/10.1016/j.ceramint.2016.04.115>

12. R.S. Yadav, I. Kuřitka, J. Vilcakova, J. Havlica, L. Kalina, P. Urbánek, M. Machovsky, D. Skoda, M. Masař, M. Holec, *Ultrason. Sonochem.* **40**, 773 (2018). <https://doi.org/10.1016/j.ultsonch.2017.08.024>
13. A. Phuruangrat, W. Maisang, T. Phonkhokkong, S. Thongtem, T. Thongtem, *Russ. J. Phys. Chem. A* **91**, 951 (2017). <https://doi.org/10.1134/S003602441705003X>
14. V. Blanco-Gutiérrez, M.J. Torralvo-Fernández, R. Sáez-Puche, *J. Phys. Chem. C* **114**, 1789 (2010). <https://doi.org/10.1021/jp908395v>
15. E. Hema, A. Manikandan, M. Gayathri, M. Durka, S. Antony, B. Venkatraman, *J. Nanosci. Nanotechnol.* **16**, 5929 (2016)
16. Y.B. Kannan, R. Saravanan, N. Srinivasan, I. Ismail, *J. Magn. Magn. Mater.* **423**, 217 (2017)
17. A. Manikandan, J. Judith Vijaya, M. Sundararajan, C. Meganathan, L.J. Kennedy, M. Bououdina, *Superlattices Microstruct.* **64**, 118 (2013). <https://doi.org/10.1016/j.spmi.2013.09.021>
18. W. Zhang, Y. Shen, J. Zhang, H. Bi, S. Zhao, P. Zhou, C. Han, D. Wei, N. Cheng, *Appl. Surf. Sci.* **470**, 581 (2019). <https://doi.org/10.1016/j.apsusc.2018.11.164>
19. A. Manikandan, L.J. Kennedy, M. Bououdina, J.J. Vijaya, *J. Magn. Mater.* **349**, 249 (2014). <https://doi.org/10.1016/j.jmmm.2013.09.013>
20. I. Quinzeni, V. Berbenni, D. Capsoni, M. Bini, *J. Solid State Electrochem.* **22**, 2013 (2018)
21. A. Ruffo, M.C. Mozzati, B. Albin, P. Galinetto, M. Bini, *J. Mater. Sci. Mater. Electron.* **31**, 18263 (2020). <https://doi.org/10.1007/s10854-020-04374-8>
22. A. Kheradmand, O. Vahidi, S.M. Masoudpanah, *Appl. Phys. A* **124**, 1 (2018). <https://doi.org/10.1007/s00339-018-1672-8>
23. G. Zou, H. Li, Y. Zhang, K. Xiong, Y. Qian, *Nanotechnology* **17**, S313 (2006). <https://doi.org/10.1088/0957-4484/17/11/S14>
24. T.J.B. Holland, S.A.T. Redfern, *Mineral. Mag.* **61**, 65 (1997). <https://doi.org/10.1180/minmag.1997.061.404.07>
25. L. Weil, F. Bertaut, L. Bochirol, *J. Phys. Le Radium* **11**, 208 (1950). <https://doi.org/10.1051/jphysrad:01950001105020800>
26. H.M. Rietveld, *J. Appl. Cryst.* **2**, 65 (1969). <https://doi.org/10.1107/S0021889869006558>
27. V. Petricek, M. Dušek, L. Palatinus, *Zeitschrift Fur Krist. Cryst. Mater.* **229**, 345 (2014). <https://doi.org/10.1515/zkri-2014-1737>
28. S.F. Gull, G.J. Daniell, *Nat.* **272**, 686 (1978). <https://doi.org/10.1038/272686a0>
29. M.C. Robert, R. Saravanan, *Powder Technol.* **197**, 159 (2010). <https://doi.org/10.1016/j.powtec.2009.09.009>
30. K. Momma, F. Izumi, *J. Appl. Cryst.* **41**, 653 (2008). <https://doi.org/10.1017/S088571561300002X>
31. K. Momma and F. Izumi, *Urn: ISSN:0021-8898* **41**, 653 (2008). <https://doi.org/10.1107/S0021889808012016>
32. J. Wan, X. Jiang, H. Li, K. Chen, *J. Mater. Chem.* **22**, 13500 (2012). <https://doi.org/10.1039/C2JM30684K>
33. J. Mangaiyarkkarasi, R. Saravanan, M.M. Ismail, *J. Chem. Sci.* **128**, 2016 (2016). <https://doi.org/10.1007/s12039-016-1190-1>
34. G.K. Williamson, W.H. Hall, *Acta Metall.* **1**, 22 (1953). [https://doi.org/10.1016/0001-6160\(53\)90006-6](https://doi.org/10.1016/0001-6160(53)90006-6)
35. S.M. Patange, S.E. Shirsath, S.S. Jadhav, K.M. Jadhav, *Phys. Status Solidi* **209**, 347 (2012). <https://doi.org/10.1002/pssa.201127232>
36. V.K. Lakhani, T.K. Pathak, N.H. Vasoya, K.B. Modi, *Solid State Sci.* **13**, 539 (2011). <https://doi.org/10.1016/j.solidstateciences.2010.12.023>
37. K.E. Sickafus, J.M. Wills, N.W. Grimes, *J. Am. Ceram. Soc.* **82**, 3279 (1999). <https://doi.org/10.1111/j.1151-2916.1999.tb02241.x>
38. D.D. Andhare, S.A. Jadhav, M.V. Khedkar, S.B. Somvanshi, S.D. More, K.M. Jadhav, *J. Phys. Conf. Ser.* **1644**, 012014 (2020). <https://doi.org/10.1088/1742-6596/1644/1/012014>
39. F.H. Cocks, *J. Mater. Sci.* **7**, 771 (1972). <https://doi.org/10.1007/BF00549905>
40. C. Choodamani, G.P. Nagabhushana, S. Ashoka, B. Daruka Prasad, B. Rudraswamy, G.T. Chandrappa, *J. Alloys Compd.* **578**, 103 (2013). <https://doi.org/10.1016/j.jallcom.2013.04.152>
41. H. Tokoro, J. Fukui, K. Watanabe, M. Yoshikiyo, A. Namai, S.I. Ohkoshi, *RSC Adv.* **10**, 39611 (2020). <https://doi.org/10.1039/D0RA07256G>
42. K. Zhang, R. Xu, C. Zhen, Y. Wu, G. Li, L. Ma, D. Hou, *Comput. Mater. Sci.* **136**, 126 (2017). <https://doi.org/10.1016/j.commatsci.2017.04.027>

Publisher's Note Springer Nature remains neutral with regard to jurisdictional claims in published maps and institutional affiliations.